 CMES, vol.104, no.1, pp.41-68, 2015

Numerical Simulation of Bubble Formation at a Single Orifice in Gas-fluidized Beds with Smoothed Particle Hydrodynamics and Finite Volume Coupled Method

F.Z. Chen[1,2], H.F. Qiang[1] and W.R. Gao[1]

Abstract: A coupled method describing gas–solid two-phase flow has been proposed to numerically study the bubble formation at a single orifice in gas-fluidized beds. Solid particles are traced with smoothed particle hydrodynamics, whereas gas phase is discretized by finite volume method. Drag force, gas pressure gradient, and volume fraction are used to couple the two methods. The effect of injection velocities, particle sizes, and particle densities on bubble growth is analyzed using the coupled method. The simulation results, obtained for two-dimensional geometries, include the shape and diameter size of a bubble as a function of time; such results are compared with experimental data, previous numerical results, and other approximate model predictions reported in the literature. Moreover, the flow profiles of gas and particle phases and the temperature distribution by the heat transfer model around the forming bubble are also discussed. All results show that the coupled method efficiently describes of the bubble formation in fluidized beds. The proposed method is applicable for solving gas–solid two-phase flow in fluidization.

Keywords: coupled method, smoothed particle hydrodynamics, finite volume method, bubble formation, heat transfer, fluidization.

1 Introduction

As a dense gas–particle two-phase flow, bubble formation at a single orifice, is a characteristic phenomenon of fluidized bed. Bubble formation contains many excellent properties of fluidized beds, such as mass and heat transfer. Therefore, an accurate prediction of bubble characteristics is important to understand and design fluidized beds.

Bubble formation at a single orifice in a two-dimensional gas-fluidized bed has been studied experimentally, theoretically, and numerically by numerous scholars.

[1] 601 Staff Room, Xi'an Hi–Tech Institute, Xi'an, Shanxi, PRC, PC 710025.
[2] Corresponding author. Tel: 15829728486; E-mail addresses: yuebo369@163.com

Earlier researchers mainly focused on empirical and theoretical analyses. Several approximate models have been presented in the literature to describe bubble growth in gas-fluidized beds at a single orifice. Davidson and Schuler (1960) first presented a theoretical solution using potential flow theory and Darcy's law to solve the single bubble rising in an unbounded fluidized bed. Harrsion and Leung (1961) correlated the bubble volume at detachment to the gas flow rate through the orifice using Davidson's model. Nguyen and Leung (1972) and Rowe (1979) demonstrated a considerable gas leakage into the emulsion phase during bubble formation. Subsequently, Zens (1968), Yang (1984), and Caram and Hsu (1986) developed their models based on the assumption that bubble grows because of the gas injection through the orifice and gas exchange with the surrounding emulsion phase through the bubble boundary. These models have focused on predicting bubble volume and formation time.

With the development of computer hardware, numerical approaches based on computational fluid dynamics have been widely used to determine the bubble behavior in fluidized beds. Thus far, all simulations on fluidization flow are based on two methods: two-fluid model (TFM) and discrete element/particle method (DEM/DPM). The gas and discrete phases in TFM are considered to be continuous and fully interpenetrating with similar conservation equation forms. Ding et al. (1990), kuipers et al. (1992), Nieuwland et al. (1996), and Hernández–Jiménez (2013) et al. characterized the interchange caused by gas advection between the emulsion phase and the bubbles in fully bubbling beds using TFM. The effect of wall on bubble shape, detachment time, and bubble trajectory was analyzed by Kumar et al. (2013) with this model. Although the TFM approach is more feasible for practical applications to complex multi-phase flows, the discrete profiles of the particle phase, such as velocity and trajectory of an individual particle cannot be obtained. Otherwise, false diffusion easily occurs in simulation and the particle diameter variations in evaporation and combustion are difficult to be considered using this model [Ravi (2013)].

The Euler–Lagrange approach DPM has been developed to overcome the limitations of TFM and trace individual particle trajectory. In this model, gas is considered as a continuous medium, whereas the motions of discrete particles are traced individually in Lagrange coordinate and solved using the Newtonian equations of motion. The mechanism of particle–particle collisions can be described the soft or hard-sphere model. Tsuji et al. (1993), Xu and Yu (1997), and Rong et al. (2012) applied the soft-sphere model to present a bubble fluidized bed, where the velocity distributions of both phases are demonstrated. Ouyang and Li (1999), Hoomans et al. (1996), and Wu et al. (2009) predicted bubble shape with the hard-sphere model. Tsukiji and Yamamoto (2005), Guo and Xu (2010), and Watanabe et al. (2011)

have used this particle method to investigate the jet flow, flexible fiber motion in compressible swirling airflow, and other gas-liquid two-phase flows. In contrast to the continuum descriptions for particle phase, DPM can easily describe particle motions, including particle rotations and particle–particle collisions. However, for the hard-sphere model, the volume fractions of particles should be lower than 10% on binary collision assumption, whereas for the soft-sphere model, time step is extremely small for particles with large stiffness coefficient. Moreover, the hard and soft-sphere models require considerable computational effort to provide accurate numerical results. Otherwise, the macro-characteristics of particle motions cannot be predicted accurately using this approach.

As a Lagrange particle method, smoothed particle hydrodynamics (SPH) [Lucy (1977); Gingold (1977)] easily traces the material interface and particle trajectory and thus has been widely used in astrophysics problems [Thacker (1998); Rosswog (2009)], multi-phase flows [Hu (2007); Adams (2010); Qiang (2011)], and explosion and shock [Randles (1996); Liu (2003); Zhang (2011)] simulations. Vignjevic (2001) provided an overview of different types of kernel interpolation used in the SPH method: conventional SPH, normalised SPH (NSPH), corrected kernel SPH (CSPH) and normalised corrected kernel SPH (NCSPH). Finite volume method (FVM), as an Euler gird-based method, has more advantages in solving gas turbulence, large deformation, and chemical reaction of fluid. Considering the advantages of SPH in solving material movement, Xiong et al. (2011) and Deng et al. (2013) used SPH to solve the pseudo fluid model for discrete phase, whereas particle or grid-based method for gas phase to simulate gas–solid fluidization. However, this model does not contain a one-to-one correspondence between the SPH and actual particles. The experimentally verified correlations was used to close the solids stress terms rather than the kinetic theory of granular flow (KTGF) [Lun (1984)]. As a result, simulations and experiments have some deviations. Otherwise, the heat transfer between gas and particles and their energy are not considered. To overcome the limitations of the existing approaches, we presented a complete novel method based on KTGF called as coupling SPH–FVM for simulating bubble formation at a single orifice in gas-fluidized beds. This method with the imported heat transfer and evaporation model can be used for gas–particle two-phase flows involving particle evaporation, combustion, heat transfer, and flow processes. Moreover, the SPH–FVM coupling framework is illustrated and compared with other models. By contrast to traditional SPH, its properties are improved to suit the discrete phase named as smoothed particle hydrodynamics (SDPH); some new physical quantities characterized by one SPH particle are added to traditional SPH parameters. The quantities of SPH particle maintain a one-to-one correspondence with those of the actual particles. With this approach, each individual particle can be traced, its infor-

mation can be obtained, and computational cost can be reduced. In this paper, we first describe the coupled method based on the pseudo-fluid model, including the heat transfer and evaporation model. Subsequently, the method is used to simulate bubble formation caused by a single jet pulse in two-dimensional coarse-particle fluidized beds. Bubble shape and diameter are compared with the experiments, as well as other simulation and theoretical results. Flow profiles, temperature distribution, and characteristics of a single particle are then discussed.

2 SPH–FVM coupling framework

Each individual particle in gas phase exhibits the properties of discrete particles. However, the whole system composed of large number of particles demonstrates the macro mechanical properties similar to gas dynamics. As a hydrodynamic method, SPH is used to determine the mathematic model of the continuum phase. SPH was first invented to solve astrophysical problems in three-dimensional open space [Lucy (1977); Gingold (1977)], including formation and collapse of galaxies, supernova explosion, collisions between planets, and evolution of the universe. The discrete stars in these problems are considered as the continuum model on macroscopic scale. An equation similar to the ideal gas equation of state is used to obtain pressure which represents the pseudo-fluid particles. Therefore, on the basis of the pseudo-model, we can couple SPH and FVM when the particle phase is treated as a pseudo-fluid. Subsequently, SPH is used to solve the pseudo-fluid model using one SPH particle to represent a specific number of discrete particles. KTGF [Lun (1984)] connects microscopic molecular dynamics with macroscopic fluid dynamics and supplies a path to implement the method. The coupling framework of the three different methods is shown in Fig.1. Particle density is described by the volume fraction in the Euler–Euler coupled approach, in which individual particle information cannot be easily obtained. In the Euler–Lagrange approach, the discrete phase is directly displaced with particles and particle collision is calculated through probabilistic model. Contact forces are calculated from the deformation contact history for the soft-sphere model, which results in large computation capacity. The interactions between particles are assumed to be pair-wise additive and instantaneous for the hard-sphere model, which then limits the application of volume fraction. In our new method, SPH is imported to represent a set of discrete particles with a diameter distribution property; this SPH differs from that of the traditional, which has been improved to SDPH for solving the discrete phase. In this model, particulate phase pressure and viscous stress depends on the fluctuating velocity of the particles, which is measured with a pseudo-temperature. By contrast to the Euler–Euler TFM, the particle distribution state can be obtained. The macro fluid dynamics properties cannot only be maintained in the particle phase,

but the differences between the particles can also reappear through Lagrange particle method. Otherwise, computational cost can be drastically reduced because discrete particles can be represented by a small quantity of SPH particles. Thus, this method can effectively simulate the gas–particle multi-phase flows in practical applications.

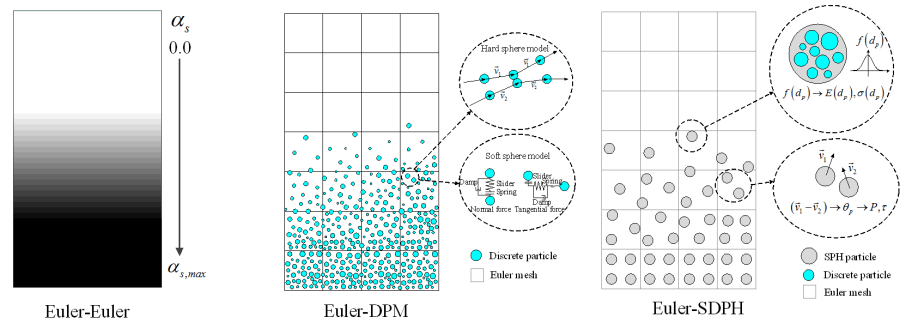

Figure 1: Schematic description of coupling framework.

Parameters such as mass, velocity, position, and pressure of the fluid on SPH particles, as well as granular profiles, including particle average diameter, diameter variance, pseudo temperature, volume fraction, and particle number represented by one SPH particle, are provided to the particles in SDPH. In traditional SPH method, the continuum fluid is discretized with a set of SPH particles and each particle occupies a geometry position. Correspondingly, numerous discrete particles are discretized with a set of SPH particles in SDPH and each particle characterizes a number of discrete particles with a specific diameter distribution. Here SPH applications can be expanded by increasing the physical quantities of SPH representation. Comparison of characteristics of SDPH and transitional SPH is shown in Fig.2. In this paper, particle average diameter, diameter variance, and particle numbers are used to represent the particle diameter distribution.

Granular pseudo-temperature, which is equivalent to the thermodynamic temperature for gases, can be introduced to determine the energy of the fluctuating velocity of the particles. Pseudo-temperature differs from the actual temperature of the discrete particles. The granular temperature (Lun, 1984) is defined as:

$$T_s = \frac{1}{3} v'^2 \tag{1}$$

where v' is the particle fluctuating velocity. Thus, granular temperature is also considered as a parameter on SPH particles. The granular temperature conservation equation is showed in the next section.

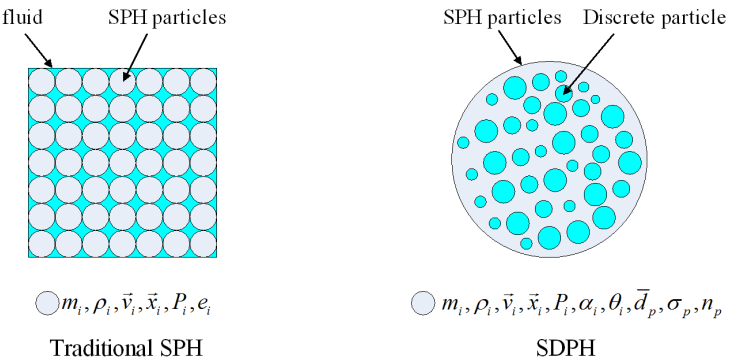

Figure 2: Comparing of characteristics of SPH particles in SDPH with traditional SPH.

The relationship between the profiles of SPH particles and that of the discrete particles is also presented. The effective density of the particle phase $\rho_{s,eff}$ for the granular pseudo-fluid is:

$$\rho_{s,eff} = \alpha_s \rho_s = \rho_{SPH} \tag{2}$$

where α_s is the volume fraction, ρ_s is the density of the particle phase, and ρ_{SPH} is the density of SPH particles.

Otherwise the mass of one SPH particle is equal to the total mass of the particle group; the density is the effective density of the discrete particles; and velocity, pseudo-temperature, and pressure are the average values of the discrete particles. Particle size distribution characters, including average diameter, variance and quantity of single particles are represented by one SPH particle.

3 Dynamic model

Mass, momentum, energy, and granular temperature transport equations for each phase are listed in Tab.1. Heat transfer and drag force between the phases are also presented.

Table 1: Model equations used for each phase in the SPH-FVM coupled method.

Mass equations		
Gas phase:	$\frac{\partial}{\partial t}(\alpha_g \rho_g) + \nabla \cdot (\alpha_g \rho_g \mathbf{v}_g) = S_g$	(T1-1)
Discrete phase:	$\frac{\partial}{\partial t}(\varepsilon_s \rho_s) + \nabla \cdot (\varepsilon_s \rho_s \mathbf{v}_s) = S_s$	(T1-2)

Momentum equations

Gas phase: $\frac{\partial}{\partial t}(\alpha_g\rho_g\mathbf{v}_g)+\nabla\cdot(\alpha_g\rho_g\mathbf{v}_g\mathbf{v}_g)=-\alpha_g\nabla P+\nabla\cdot\boldsymbol{\tau}_g+\mathbf{F}_{gs}+\alpha_g\rho_g\mathbf{g}$ (T1-3)

Discrete phase: $\frac{\partial}{\partial t}(\alpha_s\rho_s\mathbf{v}_s)+\nabla\cdot(\alpha_s\rho_s\mathbf{v}_s\mathbf{v}_s)$ (T1-4)
$=-\alpha_s\nabla P-\nabla P_s+\nabla\cdot\boldsymbol{\tau}_s+\varepsilon_s\rho_s\mathbf{g}+\mathbf{F}_{sg}+\mathbf{F}_{liq,s}+\mathbf{F}_{vm,s}$

Where $\boldsymbol{\tau}_g=-\frac{2}{3}(\rho_g\alpha_g k_g+\rho_g\alpha_g\mu_{t,g}\nabla\cdot\mathbf{v}_g)\mathbf{I}+\rho_g\alpha_g\mu_{t,g}(\nabla\mathbf{v}_g+\nabla\mathbf{v}^T{}_g)$ (T1-5)

$\boldsymbol{\tau}_s=\alpha_s\mu_s(\nabla\mathbf{v}_s+\nabla\mathbf{v}_s^T)+\alpha_s(\lambda_s-\frac{2}{3}\mu_s)\nabla\cdot\mathbf{v}_s\mathbf{I}$ (T1-6)

Turbulent viscosity

$\mu_{t,g}=\rho_g C_\mu\frac{k_g^2}{\varepsilon_g}$ (T1-7)

$k-\varepsilon$ model $\frac{\partial}{\partial t}(\alpha_g\rho_g k_g)+\nabla\cdot(\alpha_g\rho_g\mathbf{v}_g k_g)$ (T1-8)
$=\nabla\cdot(\alpha_g\frac{\mu_{t,g}}{\sigma_k}k_g)+\alpha_g G_{k,g}-\alpha_g\rho_g\varepsilon_g+\alpha_g\rho_g\Pi_{k,g}$

$\frac{\partial}{\partial t}(\alpha_g\rho_g\varepsilon_g)+\nabla\cdot(\alpha_g\rho_g\mathbf{v}_g\varepsilon_g)$ (T1-9)
$=\nabla\cdot(\alpha_g\frac{\mu_{t,g}}{\sigma_k}\nabla\varepsilon_g)+\alpha_g\frac{\varepsilon_g}{k_g}(C_1G_{k,g}-C_2\rho_g\varepsilon_g)+\alpha_g\rho_g\Pi_{\varepsilon,g}$

Drag force [Gidaspow (1992)]

$\mathbf{F}_{gs}=-\mathbf{F}_{sg}=\beta_{gs}(\mathbf{v}_g-\mathbf{v}_s)$ (T1-10)

$\beta_{gs}=\begin{cases}\beta_{Ergun}=150\frac{\alpha_s^2\mu_g}{\alpha_g d_s^2}+1.75\frac{\alpha_s\rho_g}{d_s}|\mathbf{v}_g-\mathbf{v}_s|, & \alpha_g<0.8\\ \beta_{Wen-Yu}=\frac{3}{4}C_D\frac{\alpha_s\alpha_g\rho_g}{d_s}|\mathbf{v}_g-\mathbf{v}_s|\,\alpha_g^{-2.65}, & \alpha_g\geq 0.8\end{cases}$ (T1-11)

$C_D=\begin{cases}\frac{24}{\alpha_g Re_s}[1+0.15(\alpha_g Re_s)^{0.687}] & Re_s<1000\\ 0.44 & Re_s\geq 1000\end{cases}$, (T1-12)

$Re_s=\frac{\rho_g d_s|\mathbf{v}_g-\mathbf{v}_s|}{\mu_g}$

The switch function

$\varphi_{gs}=\frac{\arctan[150\times1.75(0.2-\alpha_s)]}{\pi}+0.5$ (T1-13)

$\beta_{gs}=(1-\varphi_{gs})\beta_{Ergun}+\varphi_{gs}\beta_{Wen-Yu}$ (T1-14)

Energy equations

Gas phase: $\frac{\partial}{\partial t}(\alpha_g\rho_g h_g)+\nabla\cdot(\alpha_g\rho_g h_g\mathbf{v}_g)$ (T1-15)
$=-\nabla\cdot\alpha_g\cdot\mathbf{q}_g+\varepsilon(T_s-T_g)+\tau_g\cdot\nabla\cdot\mathbf{v}_g+\alpha_g[\frac{\partial}{\partial t}p+\mathbf{v}_g\nabla p]$

Discrete phase: $\frac{\partial}{\partial t}(\alpha_s\rho_s h_s)+\nabla\cdot(\alpha_s\rho_s h_s\mathbf{v}_s)$ (T1-16)
$=-\nabla\cdot\alpha_s\cdot\mathbf{q}_s+\varepsilon(T_g-T_s)+\tau_s\cdot\nabla\cdot\mathbf{v}_s+\alpha_s[\frac{\partial}{\partial t}p+\mathbf{v}_s\nabla p]$

Where $h_i=\int_{T_{ref}}^{T}c_{s,i}dT_i,\quad\mathbf{q}=-\kappa_i\nabla T_i$ (T1-17)

Volumetric heat transfer coefficient

$\varepsilon=\frac{6(1-\alpha_g)\alpha_g}{d_s}\varepsilon_{gs}$ (T1-18)

Nusselt number [Gunn (1978)]

$N_u=\frac{\varepsilon_{gs}d_s}{k_g}=(7-10\alpha_g+5\alpha_g^2)\left[1+0.7(\alpha_g Re_s)^{0.2}(Pr)^{1/3}\right]$ (T1-19)
$+(1.33-2.40\alpha_g+1.20\alpha_g^2)(\alpha_g Re_s)^{0.7}(Pr)^{1/3}$

Prandtl number $Pr=\frac{c_{s,g}\mu_g}{k_g}$ (T1-20)

Granular temperature conservation equation [Lun (1984)]

$\frac{3}{2}[\frac{\partial}{\partial t}(\rho_s a_s T_s)+\nabla\cdot(\rho_s a_s\mathbf{v}_s T_s)]$ (T1-21)
$=(-p_s\mathbf{I}+\tau_s):\nabla\mathbf{v}_s+\nabla\cdot(k_{T_s}\nabla T_s)-\gamma T_s+\phi_{gs}$

Diffusion coefficient	$k_{T_s} = \frac{25\rho_s d_s\sqrt{(T_s\pi)}}{64(1+e_{ss})g_{0,ss}}[1+\frac{6}{5}a_s g_{0,ss}(1+e_{ss})]^2$	
[Gidaspow (1992)]	$+2\rho_s\alpha_s^2 d_s(1+e_{ss})g_{0,ss}\sqrt{(\frac{T_s}{\pi})}$	(T1-22)
Collisional dissipation of energy [Lun (1984)]		
	$\gamma_{T_s} = \frac{12(1-e_{ss}^2)g_{0,ss}}{d_s\sqrt{\pi}}\rho_s a_s T_s^{3/2}$	(T1-23)
The transfer of the kinetic energy		
	$\phi_{gs} = -3\beta_{gs}T_s$	(T1-24)
The pseudo fluid pressure [Lun (1984)]		
	$p_s = a_s\rho_s T_s + 2\rho_s(1+e_{ss})a_s^2 g_{0,ss}T_s, \quad g_{0,ss} = \frac{s+d_s}{s}$	(T1-25)
Solids shear viscosity	$\mu_s = \mu_{s,col} + \mu_{s,kin} + \mu_{s,fr}$	(T1-26)
Collisional viscosity [Lun (1984)]		
	$\mu_{s,col} = \frac{4}{5}a_s\rho_s d_s g_{0,ss}(1+e_{ss})(\frac{T_s}{\pi})^{1/2}$	(T1-27)
Kinetic Viscosity [Gidaspow (1992)]		
	$\mu_{s,kin} = \frac{10\rho_s d_s\sqrt{T_s\pi}}{96a_s(1+e_{ss})g_{0,ss}}[1+\frac{4}{5}g_{0,ss}a_s(1+e_{ss})]^2$	(T1-28)
Frictional Viscosity [Schaeffer (1987)]		
	$\mu_{s,fr} = \frac{p_s\sin\phi}{2\sqrt{I_{2D}}}$	(T1-29)
Bulk Viscosity [Lun (1984)]		
	$\lambda_s = \frac{4}{3}a_s\rho_s d_s g_{0,ss}(1+e_{ss})(\frac{T_s}{\pi})^{1/2}$	(T1-30)

Droplet vaporization law is applied to predict vaporization from a discrete-phase particle. After reaching the vaporization temperature T_{vap} the particle temperature continues to increase until the boiling point T_{bp} is reached or until the volatile fraction is completely consumed:

$$T_{vap} \le T_s \le T_{bp} \quad \text{and} \quad m_s > (1-f_{v,0})\,m_{s,0} \tag{3}$$

The mass of the droplet is reduced:

$$\frac{dm_s}{dt} = -N_i A_s M_{w,i} \tag{4}$$

where $M_{w,i}$ is the molecular weight of the species i, m_s is the mass of the particle, and A_s is the surface area of the particle. The rate of vaporization N_i is governed by gradient diffusion, and the flux of droplet vapor into the gas phase is related to the gradient of the vapor concentration between the droplet surface and the bulk gas:

$$N_i = k_i\,(C_{i,s} - C_{i,g}) \tag{5}$$

where $C_{i,s}$ is the vapor concentration on the particle surface, $C_{i,g}$ is the vapor concentration in the bulk gas. Thus,

$$C_{i,s} = \frac{p_{sat}\,(T_s)}{RT_s}, \quad C_{i,g} = X_i\frac{p_{op}}{RT_g} \tag{6}$$

where X_i is the local bulk mole fraction of the species i, p_{op} is the local absolute pressure, and T_g is the local bulk temperature in the gas. The mass transfer coefficient k_i in Eq.5 is calculated from the Sherwood number correlation [Ranz (1952)]:

$$Sh_{AB} = \frac{k_i d_s}{D_{i,m}} = 2.0 + 0.6 Re_d^{1/2} Sc^{1/3} \tag{7}$$

where $D_{i,m}$ is diffusion coefficient of the vapor in the bulk, Sc is the Schmidt number: $Sc = \mu / \rho D_{i,m}$, and d_s is the particle diameter.

Particle vaporization can alter momentum and energy, and the changes are added to their equations as source terms. Momentum transfer is

$$\frac{d\mathbf{v}_i}{dt} = \frac{dm_{s,i}}{dt}\mathbf{v}_i \tag{8}$$

Latent heat transfer is

$$\frac{dh_i}{dt} = \frac{dm_{s,i}}{dt} h_{fg} \tag{9}$$

where h_{fg} is the latent heat.

Species mass is added to the species transport equations as a mass source.

$$\frac{\partial}{\partial t}(\rho Y_i) + \nabla \cdot (\rho \mathbf{v} Y_i) = -\nabla \mathbf{J}_i + R_i + S_i \tag{10}$$

where Y_i is the local mass fraction of the species i, R_i is the net production rate of the species i provided by the chemical reaction, S_i is the creation rate added from the dispersed phase Eq.4, and $\mathbf{J}_\mathrm{i}$ is the diffusion flux of species.

4 Numerical method

4.1 FVM for gas phase

Gas phase is solved with FVM [Parankar (1980)]. The discretized schemes of convective fluxes, diffusive fluxes, and unsteady terms are of second-order accuracy. The Semi-implicit method for pressure-linked equations (SIMPLE) algorithm is used to deal with the pressure-velocity coupling. When the residual errors of velocity and pressure are lower than 10^{-5}, the computation is considered to be converged.

4.2 SDPH for particle phase

SPH formation is divided into two key steps [Liu (2004)]. The first step is the integral representation or the so-called kernel approximation of field functions. The

second step is the particle approximation. In the first step, the integral representation of a function $f(\mathbf{x})$ in the volume $\Omega$is

$$\langle f(\mathbf{x})\rangle = \int_{\Omega} f(\mathbf{x}')W(\mathbf{x}-\mathbf{x}',h)d\mathbf{x}' \tag{11}$$

and in the second step, the function $f(\mathbf{x})$ and its derivative are given by

$$\langle f(\mathbf{x}_i)\rangle = \sum_{j=1}^{N} \frac{m_j}{\rho_j} f(\mathbf{x}_j) W_{ij} \tag{12}$$

$$\langle \nabla \cdot f(\mathbf{x}_i)\rangle = \sum_{j} \frac{m_j}{\rho_j} f(\mathbf{x}_j) \cdot \nabla_i W_{ij} \tag{13}$$

where $m_j, \rho_j, \mathbf{x}_j$ are the mass, density, and position vector of the particle j, respectively. Moreover, N is the number of particles within the support domain of the particle i. The angle bracket $\langle\rangle$ represents the kernel approximation operator. The smoothing function is $W_{ij} = W(\mathbf{x}_i - \mathbf{x}_j, h)$ where h is the smoothing length that defines the effect or support area of the smoothing function W and the gradient $\nabla_i W_{ij}$in the equation is evaluated at the particle i. The smoothing length $W$is defined as a third order B-spline in this paper [Monaghan (2005)]. The SPH formulation for pseudo-fluid conservation equations: (T1-2), (T1-4) , (T1-16), and (T1-21) are

$$\frac{d\rho_i}{dt} = \sum_{j=1}^{N} m_j \mathbf{v}_{ij} \cdot \nabla_i W_{ij} + S_i \tag{14}$$

$$\frac{d\mathbf{v}_i}{dt} = -\sum_{j=1}^{N} m_j \left(\frac{\sigma_i}{\rho_i^2} + \frac{\sigma_j}{\rho_j^2} + \Pi_{ij} \right) \nabla_i W_{ij} - \frac{\nabla P}{\rho_s} + \mathbf{g} + \mathbf{f}_{i,gs} + \frac{\mathbf{f}_{i,bp}}{\rho_i} \tag{15}$$

$$\frac{dh_{s,i}}{dt} = -\sum_{b} \frac{4m_j}{\rho_i \rho_j} \frac{\alpha_{s,i} k_i \alpha_{s,j} k_j}{\alpha_{s,i} k_i + \alpha_{s,j} k_j} (T_i - T_j) \frac{\mathbf{r}_{ij} \cdot \nabla_i W_{ij}}{\left(\mathbf{r}_{ij}^2 + \eta^2\right)} + \frac{\varepsilon(T_g - T_s)}{\alpha_s \rho_s} \tag{16}$$

$$\begin{aligned} \frac{dT_{si}}{dt} =& \frac{2}{3}\Big(\frac{1}{2}\sum_{j=1}^{N} m_j \mathbf{v}_{ji} \left(\frac{\sigma_i}{\rho_i^2} + \frac{\sigma_j}{\rho_j^2} - \Pi_{ij} \right) \nabla_i W_{ij} \\ &+ \sum_{j=1}^{N} m_j \left(\frac{k_{T_s}(\nabla T_s)_i}{\rho_i^2} + \frac{k_{T_s}(\nabla T_s)_j}{\rho_j^2} \right) \nabla_i W_{ij} - \gamma T_{si} - \varphi_{gs}\Big) \end{aligned} \tag{17}$$

where sum is calculated for all the SPH particles in the support domain. Stress is $\sigma = -p_p \bar{\bar{I}} + \bar{\bar{\tau}}_p$, $\mathbf{f}_{i,gs}$ is the drag force that acts on SPH particles per unit mass (introduced in section 4.4), $\mathbf{f}_{i,bp}$ is the boundary force, and Π_{ij} is the artificial viscosity

that prevents unphysical oscillations [Liu (2004)]. Moreover, ρ_i is the density of the SPH particle i (i.e. the effective density of discrete particles) and ρ_s is the actual density of discrete particles. Velocity vector is $\mathbf{v}_{ij} = \mathbf{v}_i - \mathbf{v}_j$, whereas the pseudo-temperature gradient $(\nabla T_s)_i$ is written as

$$(\nabla T_s)_i = m_i \sum_{j=1}^{N} \frac{T_{sj} - T_{si}}{\rho_{ij}} \nabla_i W_{ij} \tag{18}$$

4.3 SPH–FVM coupling approach

The particle quantities of heat, mass, and momentum is gained or lost under the effect of drag force, pressure and heat transfer from the gas. These quantities are also reacted on the continuum phase. When particle temperature reaches the vaporization temperature, the mass exchange between gas and particle occurs. The continuous phase affects the discrete phase, whereas the discrete phase also reacts in the continuous phase. This two-way coupling is accomplished by alternately solving the discrete and continuous phase equations until their solutions remain constant.

The solution procedure for the SPH–FVM coupling algorithm containing the heat transfer and evaporation model is shown in Fig.3. First, the gas velocity, pressure gradient, and temperature on meshes are interpolated to the SPH particle positions to obtain the virtual values of the gas. Subsequently, these values are used to determine the effect of drag force, pressure, and heat convection on SPH particles by the gas. These parameters are added to the momentum and energy equations as source terms to update the velocity and temperature of SPH particles. Second, the updated velocity and temperature of SPH particles are interpolated to the meshes using the same method. These values are used to calculate the drag force and heat convection from the particles to gas and then to update the velocity and temperature of the flow field. During this iteration, the velocity and temperature of flow field is updated at any moment, whereas the particle velocity and temperature obtained through interpolation remain constant until convergence. At $Tem > Tem_{sat}$, the particles start to evaporate. The volatilized quantity of each particle is calculated with the SPH program and then used to update the SPH mass, momentum and energy equations. The diameter distribution of the particles represented by SPH and the volume fraction of each phase are also improved. The volatilized species content is obtained through each particle evaporation and particles property in each mesh. The result is used to calculate the species transport equations and obtain the spatial distribution of each gas species.

The drag force that functions on a particle in gas–particle systems can be represented by the product of the momentum transfer coefficient β_{gs} and the slip velocity

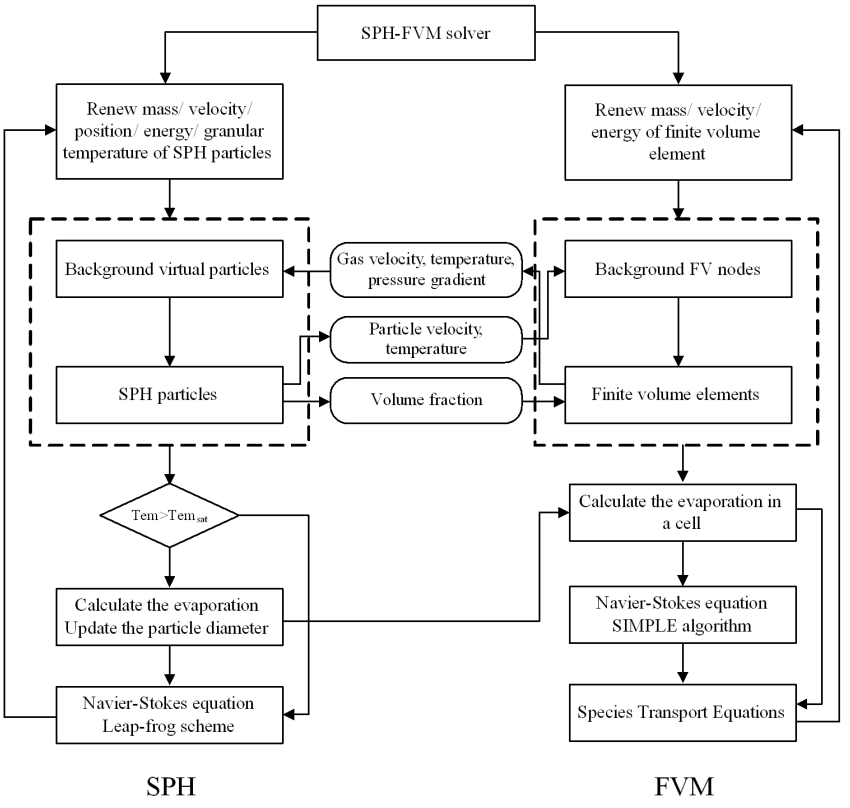

Figure 3: Solution procedure for SPH-FVM coupling algorithm.

$\mathbf{v}_g - \mathbf{v}_s$ between the two phases (Eq.T1-10). The drag force on one discrete particle per unit mass is

$$\mathbf{f}_{gs} = \frac{\beta_{gs}\left(\mathbf{v}_g - \mathbf{v}_s\right)}{a_s \rho_s} \tag{19}$$

One SPH particle represents a series of discrete particles with different diameters. Thus, the drag force on one SPH particle per unit mass should be expressed by

$$\mathbf{f}_{gs,SPH} = \frac{\mathbf{F}_{gs,SPH}}{m_{SPH}} = \frac{\sum_k^N \mathbf{F}_{gs,k}}{\sum_k^N m_k}, \quad \text{and} \quad m_k = \rho_s \left(\frac{\pi d_s^2}{4}\right) \text{ for 2D.} \tag{20}$$

where $\mathbf{F}_{gs,k}$ is the drag force on the discrete particle$k$, and N is the number of granule within one SPH particle.

Another important parameter is the volume fraction of gas α_p, which is computed by SPH. As introduced in Sec.2, the density of SPH particle is similar to the effective density of discrete particles. Thus, the volume fraction of the discrete particle i is

$$\alpha_{si} = \frac{\rho_{SPH}}{\rho_s} \tag{21}$$

and the gas volume fraction at the same position is

$$\alpha_{gi} = 1 - \frac{\rho_{SPH}}{\rho_s} \tag{22}$$

The obtained volume fraction is used to calculate the gas volume fraction at the center of the grid through interpolation.

The data between SPH particles and FVM meshes are exchanged with the method of kernel function interpolation. The kernel function is

$$f(\mathbf{r}_s) = \sum_g \frac{m_g}{\rho_g} f(\mathbf{r}_g) W_{sg}(\mathbf{r}_s - \mathbf{r}_g, h) \tag{23}$$

This function is similar to the SPH interpolation function (Eq.12). To improve the particle inconsistency that resulted from truncation of the smoothing function by the boundary, we used a normalization formulation derived by Randles and Libersky (1996)

$$f(\mathbf{r}_s) = \frac{\sum_g \frac{m_g}{\rho_g} f(\mathbf{r}_g) W_{sg}(\mathbf{r}_s - \mathbf{r}_g, h)}{\sum_g \frac{m_g}{\rho_g} W_{sg}(\mathbf{r}_s - \mathbf{r}_g, h)} \tag{24}$$

Fig.4 represents the interpolation strategy of the velocity between meshes and particles. Temperature, pressure gradient and volume fraction are interpolated using similar method.

4.4 Boundary conditions

(1) SPH boundary conditions

For SPH method, the enforcement of contact condition is difficult due to the lack of a finite element like Kronecker delta condition. Thus, we use a penalty function [Li (2002)] to obtain the interaction force through the nodal integration from the variation of penalty potentials. The kinematics contact condition is enforced by a penalty potential $\prod$ defined as

$$\prod = \frac{\varepsilon}{2} \int_\Gamma (\vec{\boldsymbol{v}}_f \cdot \vec{\boldsymbol{n}} - \vec{\boldsymbol{v}}_r \cdot \vec{\boldsymbol{n}})^2 d\Gamma \tag{25}$$

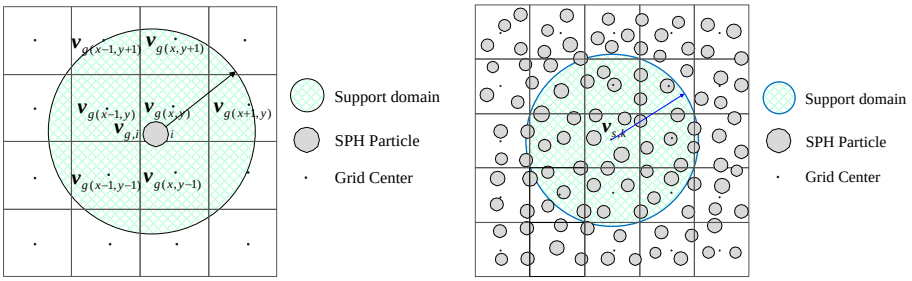

(a) $\boldsymbol{v}_{g,i}$ interpolated from the meshes (b) $\boldsymbol{v}_{s,k}$ interpolated from the particles

Figure 4: Interpolation strategy between meshes and particles.

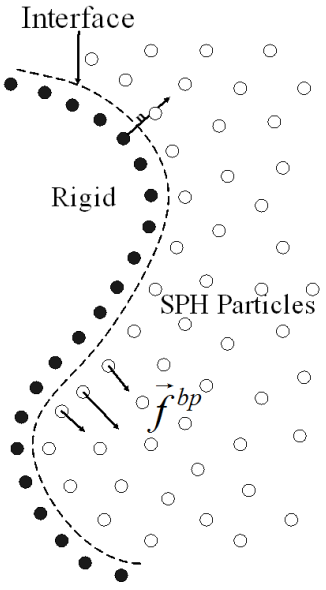

Figure 5: SPH particles and rigid interaction.

where ε the is penalty parameter and Γ is the interface. The variation of the Eq. (22) is written as

$$\delta\prod = \varepsilon\int_{\Gamma}\delta\hat{\boldsymbol{v}}_f\cdot\vec{\boldsymbol{n}}(\vec{\boldsymbol{v}}_f\cdot\vec{\boldsymbol{n}}-\vec{\boldsymbol{v}}_r\cdot\vec{\boldsymbol{n}})d\Gamma \tag{26}$$

where the test function $\delta\hat{\boldsymbol{v}}_f$ is given by $\delta\hat{\boldsymbol{v}}_f = \sum_i \delta\vec{\boldsymbol{v}}_f W$ and the community part $\sum_i \delta\vec{\boldsymbol{v}}_f$ can be deleted on the Galerkin formulation of SPH. Derivation process can be obtained in the literature [Gallati (2002)]. Using nodal integration, the face f_i^{bp} at the interface particle i of fluid is

$$f_i^{bp} = -\varepsilon\sum_{j\in B}\left((\vec{\boldsymbol{v}}_i-\vec{\boldsymbol{v}}_j^B)\cdot\vec{\boldsymbol{n}}_j W_{ij}A_j\vec{\boldsymbol{n}}_j\right) \tag{27}$$

where ε is the penalty parameter, B is the set of particles from the rigid surface and the superscript B denotes the interface between fluid and structure. The boundary weight A_j is associated with the boundary particle j.

The penalty parameter is important in this method because of it directly affects the condition number of the resulting system. System condition worsens when the values for the parameter increases. Therefore, penalty parameter is designed to change with the relative distances to maintain algorithm stability and to select the parameters easily. We replace ε by $\varepsilon(2h)/|\mathbf{r}|$ and $2h$ is the searching field of the nearest neighbor particles. The force formulation is written as

$$\vec{\boldsymbol{f}}_i^{bp} = \begin{cases} -\varepsilon 2h_i\sum\limits_{j\in B}\left(\frac{1}{|\vec{\boldsymbol{r}}_{ij}|}(\vec{\boldsymbol{v}}_i-\vec{\boldsymbol{v}}_j^B)\cdot\vec{\boldsymbol{n}}_j W_{ij}A_j\vec{\boldsymbol{n}}_j\right) & \vec{\boldsymbol{v}}_i\cdot\vec{\boldsymbol{n}}_j<0 \\ 0 & \vec{\boldsymbol{v}}_i\cdot\vec{\boldsymbol{n}}_j\geq 0 \end{cases} \tag{28}$$

In this formulation, interaction occurs when the particles of fluid and rigid are close to each other but vanishes when the particles are far from each other. This formation maintains the dynamics contact condition. Moreover, the interaction between SPH particles and rigid is shown in Fig.5.

In addition, the initial solid velocity in the bed is zero.

(2) FVM boundary conditions

Along the wall, no-slip condition is assumed for the gas phase $u_{gx}=u_{gy}=u_{gz}=0$.

At the entrance, the gas is injected along the axial direction. At the outlet, an outflow boundary condition is provided, in which the velocity gradient is zero, i.e., $\partial u_x/\partial x = 0$.

5 Problem description

Fig.6 shows the initial and boundary conditions used for the numerical simulation of bubble formation in gas-fluidized beds with one central orifice (Nieuwland, 1996). The wall of the bed is modeled as a non-slip rigid wall for both phases. At the center of the bed the gas is insufflated to the beds through the orifice. At the top of the bed, outflow boundary is assumed for fluid and particle phases. A free-board with a height similar to that of the initial bed is provided for bed expansion. In accordance with the experimental condition, minimum fluidization is prescribed as the initial condition for numerical calculations. At zero time, the velocity of the gas injected through the central orifice increases instantaneously from the minimum fluidization velocity v_{mf} to the required orifice velocity v_{inj}. Three orifice velocities (i.e., 10, 15, and 20m/s) are considered in this study. SPH particles are distributed in the bed, whereas FVM grids are placed in the whole field with quadrilateral elements as shown in Fig.6(b). The parameters in this simulation are listed in Tab.2.

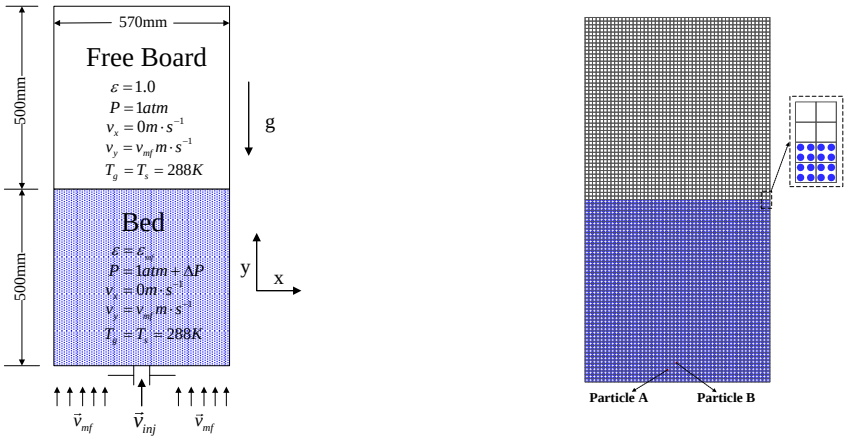

(a) Geometry (b) Numerical grids and particles

Figure 6: Geometry of the bed and numerical grids and particles.

6 Results and discussion

We use B-spline kernel [Monaghan (2005)] as the weighted function, list neighbor searching method [Liu (2004)], and leap-frog method to update the physical variables of SPH particles in all cases. Artificial viscosity parameters are $\alpha = 0.1$

Table 2: Parameters for bubble simulation.

Parameters	Description	Value
$\rho_g(kg/m^3)$	Gas density	1.225
$\mu_g(Pa \cdot s)$	Gas viscosity	1.7895E–05
$\rho_p(kg/m^3)$	Solid density	3060
$d_p(mm)$	Particle diameter	0.285
α_p	Packing volume fraction	0.55
$r_{inj}(mm)$	Orifice width	15
$v_{inj}(m/s)$	Injection velocity	5.0, 10.0, 15.0
$v_{mf}(m/s)$	Minimum fluidization velocity	0.08
n	Particles number represented by one SPH particle	220
$d_{av}(mm)$	Particles average diameter represented by one SPH particle	0.285
$\Delta x_{sph}(mm)$	SPH particle distance	5.7
$h(mm)$	SPH smoothing length	8.55
$\rho_{SPH}(kg/m^3)$	SPH particle density	1683
$\Delta x \times \Delta y(mm)$	FVM grid spacing	11.4×11.4
$\Delta T_{FVM}(s)$	FVM time step	5×10^{-5}

and $\beta = 0.2$. Smoothing length is 1.5 times higher than particle diameter. Penalty parameter is $\varepsilon = 10^3$.

6.1 Bubble formation

The comparisons of bubble shape during its formation using the new method with TFM and experimental results are shown in Fig.7. As the time increases, the bubble is formed gradually from the orifice. At 0.2s the bubble grows to its maximum size. Subsequently, the bubble is detached from the bottom of the bed and the bubble wake follows. The pictures shows that the shape of the bubble is qualitatively consistent with the results of TFM and previous experiments [Nieuwland (1996)].

To determine the bubble diameters from the numerically calculated porosity distributions, we define the bubble contour as a void fraction of 0.85 in the present study. This particular selection defines the bubble boundary as a contour with very strong porous gradients, particularly near the bubble base. The contour is defined as the diameter of a circle with similar area to the numerical simulating area S with $\alpha_g > 0.85$ for two-dimensional geometry. The expression for the equivalent bubble

diameters in two-dimensional case is:

$$D_e = \sqrt{\frac{S}{0.25\pi}} \tag{29}$$

These curves characterize these relationships, as shown in Fig.8. The theoretically calculated bubble size from the SPH-FVM coupled method is consistent with the experimental data, and its accuracy is higher than other traditional computational models. A total of 220 solid particles are characterized by one SPH particle; thus, the computational cost is significantly reduced.

6.2 Effect of jet velocity and particle properties

To investigate the effect of jet velocity, we select three different injection rates ($v_{inj} = 10, 15, 20 m/s$) for comparisons. Fig.9 shows the comparison of the equivalent bubble diameter with these three different injection rates. It can be seen a high injection rate results in large bubble diameter.

Fig.10 demonstrates the variations in the equivalent bubble diameter for different particle properties, including diameter and density. The main parameters for case simulations are listed in Tab.3. Case A and B have similar curves, in which a similar minimum fluidization velocity is used. Thus, the effect of the minimum fluidization velocity on this process is related to the effect of particle size and particle density on bubble formation. This result is consistent with the conclusion reported by Nieuwland et al. (1996). Moreover, the result demonstrates that a low minimum fluidization velocity results in large bubble size using a constant jet velocity.

Table 3: Particle properties.

Cases	Particle diameter (mm)	Particle density (kg/m^3)	Minimum fluidization velocity (m/s)
A	285	3060	0.080
B	460	1435	0.096
C	140	2920	0.019

6.3 Gas and particle flow field

The velocity vector and the stream-tracers for the gas phase at different time steps during bubble formation are shown in Fig.11. Bubble necking stars when the bubble grows and the neck width decreases with the increasing time step. During neck formation, the surrounding fluid rushes to the detachment point and creates a strong

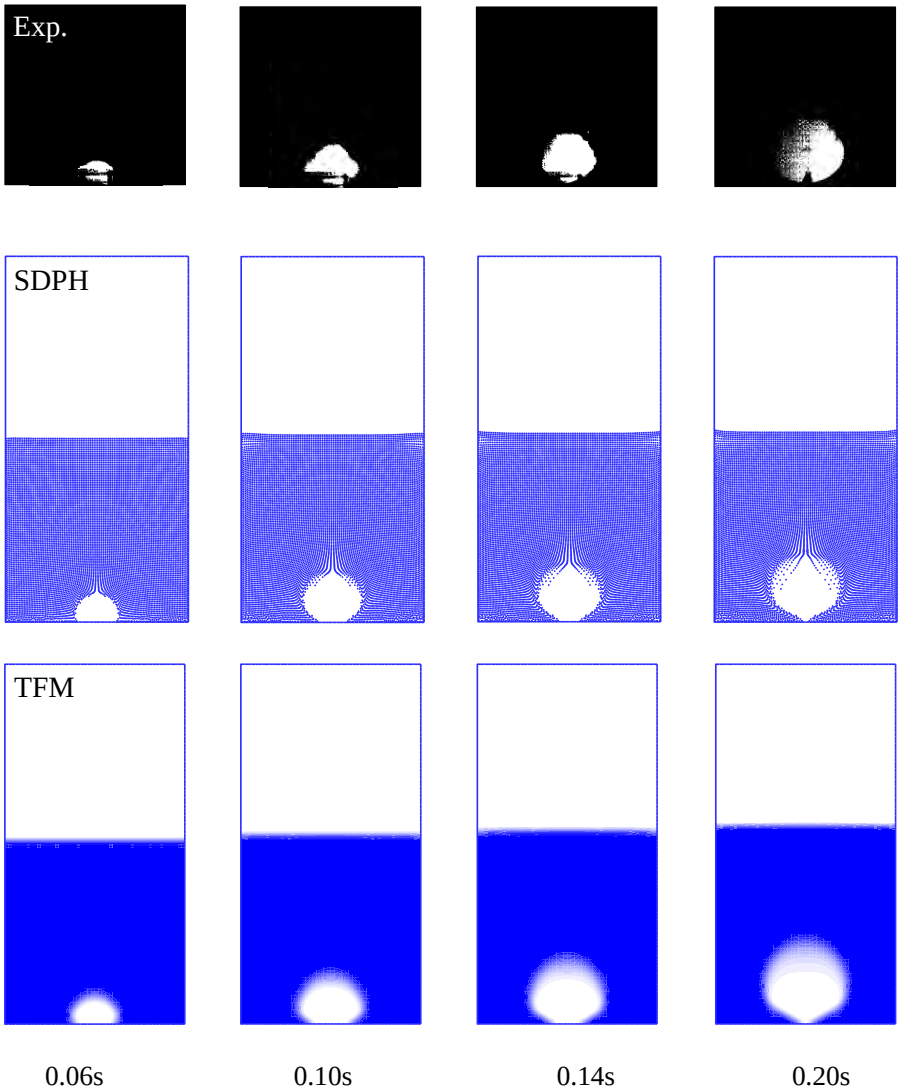

Figure 7: Experimentally observed (Nieuwland, 1996) and numerical calculated bubble growth at a single orifice in a two-dimensional gas-fluidized bed with SDPH and TFM method.

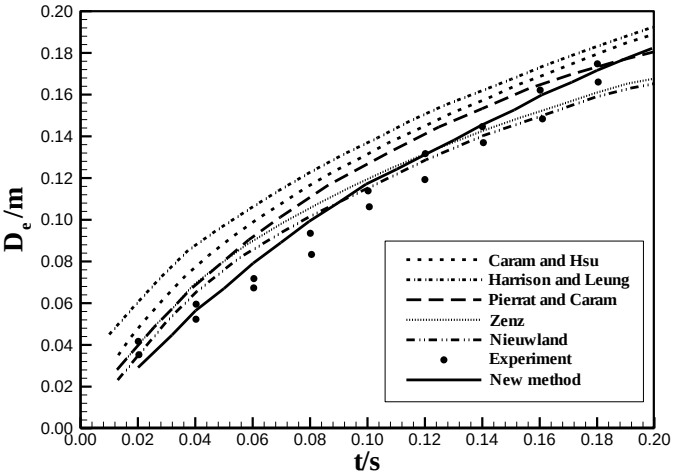

Figure 8: Experimentally observed (Nieuwland,1996) and numerical calculated bubble growth at a single orifice in a two-dimensional gas-fluidized bed with SDPH and other phenomenological models.

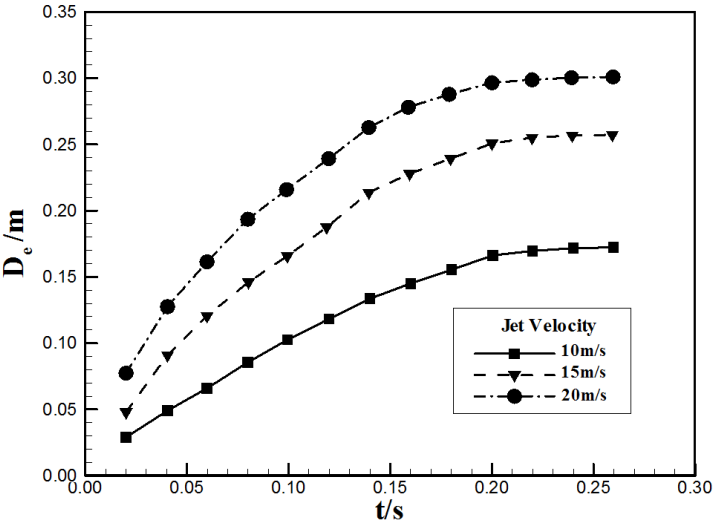

Figure 9: Equivalent bubble diameter for beds with different jet velocities.

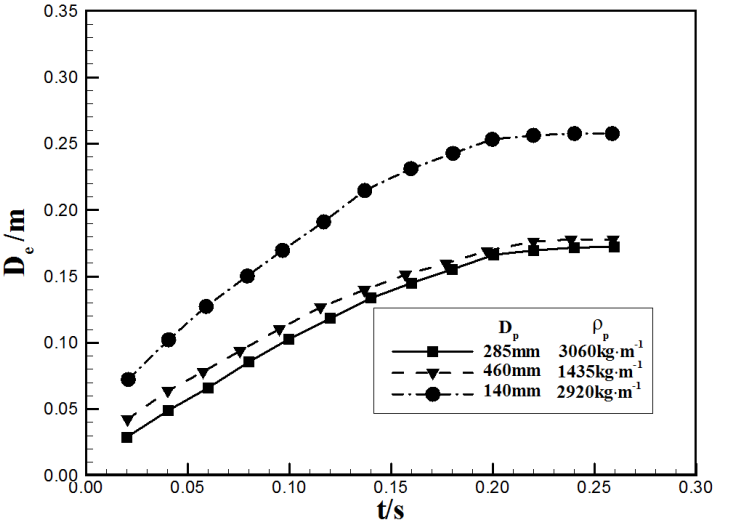

Figure 10: Equivalent bubble diameter for beds with different particle properties.

localized velocity of the gas phase at the trailing edge of the bubble. The gas phase begins to slide down along the bubble periphery toward the bottom of the bubble. Thus, the onset of wake begins earlier than the detachment of the bubble. Fig.12 shows the vector plots of the particles around the forming bubble. As bubble forms, the particles move gradually to the bottom of the bubble. Simultaneously, a dilute particle layer with finite thickness covers the surface of the bed. In this layer, the particle interspaces are evidently large; hence, the outer particles of this layer are exposed to less interference and move faster than the inner particles.

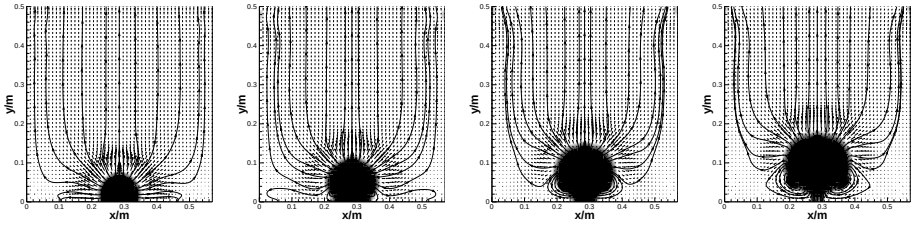

Figure 11: Stream-tracer and vector plots of the gas phase around the forming bubble for gas injection rate of 10m/s.

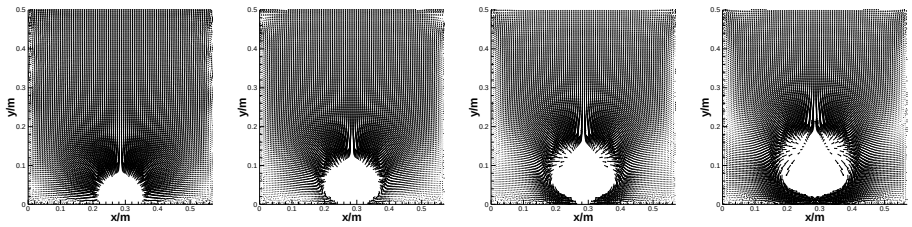

0.05s 0.10s 0.15s 0.20s

Figure 12: Vector plots of the particles around the forming bubble for gas injection rate of 10m/s.

6.4 Comparison of temperature distribution in both phases

Fig.13 and 14 show the temperature distribution of gas and particle phases at different times during the bubble formation. As the high-temperature gas is injected into the bed, the gas temperature gradually increases, whereas the particle temperature evidently increase after absorbing heat from the gas phase for the convective heat transfer between the phases. The gas temperature in the center area of the bubble can reach 345K, whereas the particle temperature in the edge of the bubble can reach 289.5K. The effect of heat transfer between particles constantly exists except for the interface heat transfer. Thus, an elevated temperature area exists for the particle phase at the edge of the bubble. The obtained result is consistent with that of the TFM. Moreover, the result of the temperature distribution of gas and particle phases is consistent using SDPH but differs from each other using TFM. Analysis shows that this difference is possibly related to the convergence of the approach which is analyzed and validated in the next step.

6.5 Particle trajectory and temperature rising curve

To analyze the properties of each single particle and trace the movement, distortion, and heat transfer of some special particles, we select two single particles at different positions of the bed. Particle A is obtained at the top of the bubble, whereas particle B at the left of the bubble. These particles are shown in Fig.6(b), whereas Fig.15(a) shows the trajectory of particle A. The particles located on both sides of the bubble gradually deviate from the center to the sport as the bubble is formed. After reaching the top of the bubble transverse, the particles start to move reversely close to its initial position. The particles continue to move from the bottom of the bed upward with the growing bubble. Finally a circular trajectory is formed. However, the particles at the top of the bubble maintain an upward trend with the bubble growing until it bursts, as shown in Fig.16(a). Fig.15(b) and Fig.16(b) demonstrate

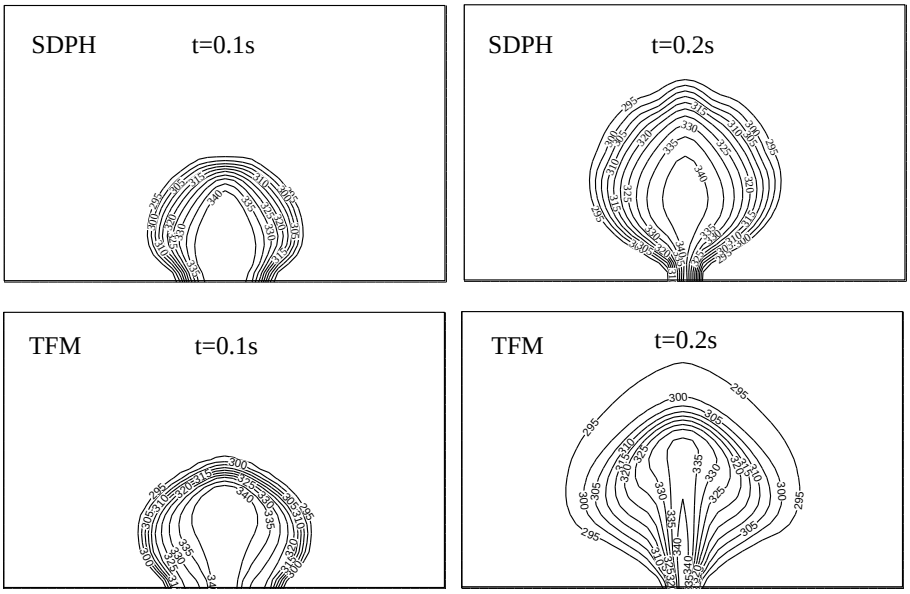

Figure 13: Comparison of temperature distribution of the gas phase during the bubble formation.

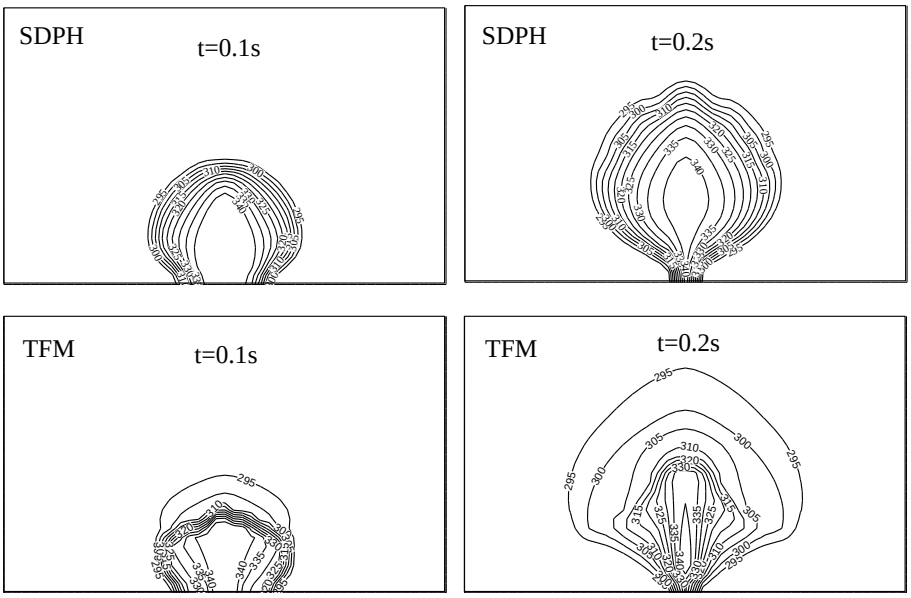

Figure 14: Comparison of temperature distribution of the particle phase during the bubble formation.

the temperature rising curve of particles A and B. The temperature of the particles located on both sides of the bubble increasing gradually caused by the effect of heat transfer from the gas phase as the bubble increases. After 0.2s the bubble deviates from the bed bottom, and its gas inside is in a closed state. The temperature of the particles and gas in the bubble gradually reach an equilibrium state, whereas the particle temperature remains constant. However, the temperature of the particles at the top of bubble keep still increase because of heated gas injected in the orifice.

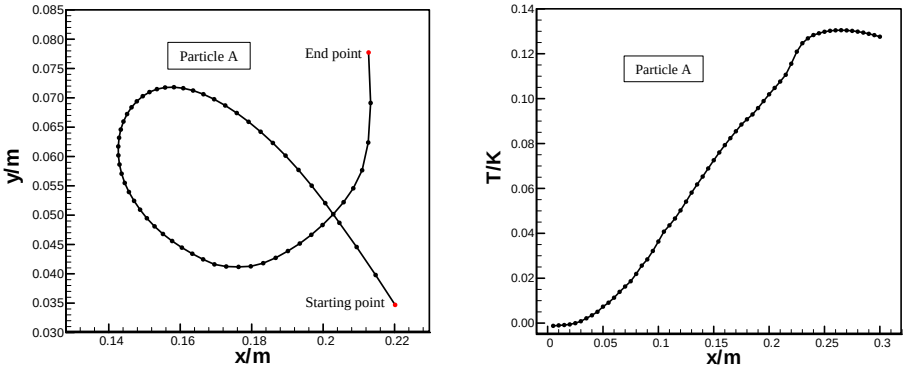

(a) particle trajectory (b) particle temperature rising curve

Figure 15: The trajectory and temperature rising curve of particle A.

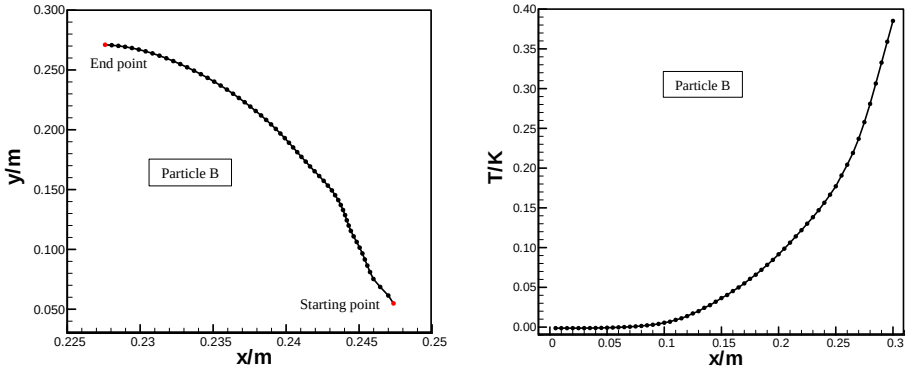

(a) particle trajectory (b) particle temperature rising curve

Figure 16: The trajectory and temperature rising curve of particle B.

7 Conclusion

An efficient SPH–FVM coupled model, including heat transfer and evaporation for bubble formation in gas-fluidized bed has been presented. SPH is used for discrete phase to trace the movement of each individual particle, whereas FVM for continue phase to compute the turbulent fluids. To represent a set of discrete particles with diameter distribution property, we improved the traditional SPH to be SDPH for solving the discrete phase. The coupling framework between the two methods is built using KTGF. Subsequently, the bubbling fluidized bed is simulated in the industrial fluidized bed. The results includes the shape and diameter size of the bubble as a function of time; such results are consistent with experimental data, previous numerical results and other approximate models reported in the literature. Moreover, a high injection rate results in large bubble diameter and for a constant jet velocity, low minimum fluidization velocity causes a larger bubble size. In addition, the trajectory and temperature rising processes are captured with this new method. Thus, the proposed method can predict the macro-characteristic parameters of particles and has advantages in tracing single particle properties.

Acknowledgement: The support of National Nature Science Foundation of China (No. 51276192), No. 61338 for the National Basic Research Program of China, and the Innovative Research Project of Xi'an Hi-tech Institute (EPXY0806) are gratefully acknowledged.

References

Adami, S.; Hu, X. Y.; Adams, N. A. (2010): A new surface-tension formulation for multi-phase SPH using a reproducing divergence approximation. *J. Comput. Phys.*, vol. 229, pp. 5011-5021.

Caram, H. S.; Hsu, K. K. (1986): Bubble formation and gas leakage in ?uidized beds. *Chem. Eng. Sci.*, vol. 41, pp. 1445-1453.

Deng, L.; Liu, Y.; Wang, W.; Ge, W.; Li, J. (2013): A two-fluid smoothed particle hydrodynamics (TF–SPH) method for gas–solid fluidization. *Chem. Eng. Sci.*, vol. 99, pp. 89-101.

Ding, J.; Gidaspow, D. (1990): A bubbling fluidization model using kinetic theory of granular flow. *AIChE. J.*, vol. 36, pp. 523-538.

Gallati, M.; Breachi, G. (2002): Numerical Description of Rapidly Varied Flows via SPH Method. *IASTED International Conference of ASM*, Creta.

Gidaspow, D.; Bezburuah, R.; Ding, J. (1992): Hydrodynamics of circulating fluidized beds, kinetic theory approach, Fluidization?. *Proceedings of the 7th En-*

gineering Foundation Conference on Fluidization, Brisbance, Australia, pp. 75-82.

Gingold, R. A.; Monaghan, J. J. (1977): Smoothed particle hydrodynamics–theory and application to non-spherical stars. *Mon Not R Astron Soc.*, vol. 181, pp. 375–389.

Gunn, D. J. (1978): Transfer of heat or mass to particles in fixed and fluidized beds. *Int. J. Heat. Mass. Tran.*, vol. 21, pp. 467-476.

Guo, H. F.; Xu, B. G. (2010): A 3D numerical model for a flexible fiber motion in compressible swirling airflow. *CMES–Comp. Model. Eng.*, vol.61, no.3, pp. 201-222.

Harrison, D.; Leung, L. S. (1961): Bubble formation at an orifice in a fluidised bed. *Chem. Eng. Res. Des.*, vol. 39, pp. 409-414.

Hernández–Jiménez, F.; Gómez–García, A.; Santana, D.; Acosta–Iborra, A. (2013): Gas interchange between bubble and emulsion phases in a 2D fluidized bed as revealed by two-fluid model simulations. *Chem. Eng. J.*, vol. 215-216, pp. 479-490.

Hoomans, B. P. B.; Kuipers, J. A. M.; Briels, W. J.; van Swaaij, W. P. M. (1996): Discrete particle simulation of bubble and slug formation in a two-dimensional gas-fluidised bed: a hard-sphere approach. *Chem. Eng. Sci.*, vol. 51, pp. 99-118.

Hu, X. Y.; Adams, N. A. (2007): An incompressible multi-phase SPH method. *J Comput Phys*, vol. 227, pp. 264-278.

Kuipers, J. A. M.; Tammes, H.; Prins, W.; van Swaaij, W. P. M. (1992): Experimental and theoretical porosity profiles in a two-dimensional gas-fluidized bed with a central jet. *Powder. Technol.*, vol. 71, pp. 87-99.

Kumar, A.; Das, S.; Fabijanic, D.; Gao, W.; Hodgson, P. (2013): Bubble-wall interaction for asymmetric injection of jets in solid-gas fluidized bed. *Chem. Eng. Sci.*, vol. 101, pp. 56-68.

Li, S.; Liu, W. K. (2002): Meshfree and Particle Methods and their Applications. *Appl. Mech. Rev.*, vol. 55, pp. 1-34.

Liu, G. R.; Liu, M. B. (2004): Smoothed particle hydrodynamics: a meshfree particle method. World Scientific, Singapore.

Liu, M. B.; Liu, G. R.; Zong, Z.; Lam, K. Y. (2003): Computer simulation of the high explosive explosion using smoothed particle hydrodynamics methodology. *Comput. Fluids.*, vol. 32, pp. 305-322.

Lucy, L. B. (1997): A numerical approach to the testing of the fission hypothesis. *Astron J*, vol. 82, pp. 1013-1024.

Lun, C. K. K.; Savage, S. B.; Jeffrey, D. J. (1984): Kinetic theories for granular

flow: inelastic particles in Couette flow and slightly inelastic particles in general flow field. *J. Fluid. Mech.*, vol. 140, pp. 223-256.

Monaghan, J.J. (2005): Smoothed particle hydrodynamics. *Rep. Prog. Phys.*, vol. 68, pp.1703-1759.

Nguyen, X. T.; Leung, L. S. (1972): A note on bubble formation at an orifice in a fluidised bed. *Chem. Eng. Sci.*, vol. 27, pp. 1748-1750.

Nieuwland, J. J.; Veenendaal, M. L.; Kuipers, J. A. M.; van Swaaij, W. P. M. (1996): Bubble formation at a single orifice in gas-fluidised beds. *Chem. Eng. Sci.*, vol. 51, pp. 4087-4102.

Ouyang, J.; Li, J. (1999): Particle-motion-resolved discrete model for simulating gas–solid fluidization. *Chem. Eng. Sci.*, vol. 54, pp. 2077-2083.

Parankar, S. V. (1980): Numerical heat transfer and fluid flow, Hemisphere, New York, 1980.

Qiang, H. F.; Chen, F. Z.; Gao, W. R. (2011): Modified Algorithm for Surface Tension with Smoothed Particle Hydrodynamics and Its Applications. *CMES–Comp. Model. Eng.*, vol. 77, pp. 239-262.

Randles, P. W.; Libersky, L. (1996): Smoothed particle hydrodynamics some recent improvements and applications. *Comput Methods Appl Mech Eng*, vol. 139, pp. 375-408.

Ranz, W. E.; Marshall, W. R. (1952): Evaporation from Drops, Part I. *Chem. Eng. Prog.*, vol. 48, pp. 141-146.

Ravi, I. S.; Anders, B.; Mikko, H. (2013): CFD modeling to study fluidized bed combustion and gasification. *Appl. Therm. Eng.*, vol. 52, pp. 585-614.

Rong, L. W.; Zhan, J. M.; Wu, C. L. (2012): Effect of various parameters on bubble formation due to a single jet pulse in two-dimensional coarse-particle fluidized beds. *Adv Powder Technol*, vol. 23, pp. 398-405.

Rosswog, S. (2009): Astrophysical smooth particle hydrodynamics. *New Astron Rev.*, vol. 53, pp. 78-104.

Rowe, P. N.; MacGillivray, H. J.; Cheesman, D. J. (1979): Gas discharge from an orifice into a gas fluidised bed. *Chem. Eng. Res. Des.*, vol. 57, pp. 194-199.

Schaeffer, D. G. (1987): Instability in the Evolution Equations Describing Incompressible Granular Flow. *J. Diff. Eq.*, vol. 66, pp. 19-50.

Thacker, R. J.; Tittley, E. R.; Pearce, F. R.; Couchman, H. M. P.; Thomas, P. A. (1998): Smoothed Particle Hydrodynamics in cosmology: a comparative study of implementations. *Mon Not R Astron Soc.*, vol. 2, pp. 1-30.

Tsuji, Y.; Kawaguchi, T.; Tanaka, T. (1993): Discrete particle simulation of two-

dimensional ?uidized bed. *Powder Technol*, vol. 77, pp. 79-87.

Tsukiji, T.; Yamamoto, Y. (2005): Computational modeling of gas-particle two-phase jet by a 3-D vortex method. *CMES–Comp. Model. Eng.*, vol. 9, no. 3, pp. 235-241.

Vignjevic, R.; Vuyst, T. De; Gourma, M. (2001): On interpolation in SPH. *CMES–Comp. Model. Eng.*, vol. 2, no. 3, pp. 319-336.

Watanabe, H.; Suzuki, M.; Ito, N. (2011): Huge-scale molecular dynamics simulation of gas-liquid two-phase flow. *ICCES-International Conference on Computational & Experimental Engineering and Science*, vol. 18, no. 2, pp. 49-49.

Wu, C. L.; Berrouk, A. S.; Nandakumar, K. (2009): Three-dimensional discrete particle model for gas–solid fluidized beds on unstructured mesh. *Chem. Eng. J.*, vol. 152, pp. 514-529.

Xiong, Q.; Deng, L.; Wang, W.; Ge, W. (2011): SPH method for two-fluid modeling of particle-fluid fluidization. *Chem. Eng. Sci.*, vol. 66, pp. 1859-1865.

Xu, B. H.; Yu, A. B. (1997): Numerical simulation of the gas–solid flow in a fluidized bed by combining discrete particle method with computational fluid dynamics. *Chem. Eng. Sci.*, vol. 52, pp. 2785-2809.

Yang, W.; Revay, D.; Anderson, R. G. (1984): Fluidization phenomena in a large-scale, cold-flow model. *Fluidization IV*, pp. 77.

Zenz, F. A. (1968): Bubble formation and grid design. *Institution of Chemical Engineers Symposium Series*, pp. 136-139.

Monaghan, J. J. (2005): Smoothed particle hydrodynamics. *Rep. Prog. Phys.*, vol. 68, pp. 1703-1759.

Zhang, Z. C.; Qiang, H. F.; Gao, W. R. (2011): Coupling of smoothed particle hydrodynamics and finite element method for impact dynamics simulation. *Eng. Struct.*, vol. 33, pp. 255-264.